Nanoscale Advances

ROYAL SOCIETY OF CHEMISTRY

PAPER

View Article Online
View Journal | View Issue

Cite this: *Nanoscale Adv.*, 2022, **4**, 3737

Mechanistic insights into Ag^+ induced size-growth from $[Au_6(DPPP)_4]^{2+}$ to $[Au_7(DPPP)_4]^{2+}$ clusters†

Ying Lv,[a] Xiaohang Wu,[a] Shuping He[a] and Haizhu Yu *[ab]

Received 12th May 2022
Accepted 2nd July 2022

DOI: 10.1039/d2na00301e

rsc.li/nanoscale-advances

The size conversion of atomically precise metal nanoclusters lays the foundation to elucidate the inherent structure–activity correlations on the nanometer scale. Herein, the mechanism of the Ag^+-induced size growth from $[Au_6(dppp)_4]^{2+}$ to $[Au_7(dppp)_4]^{3+}$ (dppp is short for 1,3-bis(diphenylphosphino)propane) is studied *via* density functional theory (DFT) calculations. In the absence of extra Au sources, the one "Au^+" addition was found to be regulated by the Ag^+ doping induced Au-activation, *i.e.*, the formation of formal Au(I) blocks *via* the Ag^+ alloying processes. The Au(I) blocks could be extruded from the core structure in the formed Au–Ag alloy clusters, triggering a facile Au^+ migration to the Au_6 precursor to form the Au_7 product. This study sheds light on the structural and stability changes of gold nanoclusters upon the addition of Ag^+ and will hopefully benefit the development of more metal ion-induced size-conversion of metal nanoclusters.

Introduction

The stimuli response upon exposure to extra metal ions represents an attractive characteristic of metal nanoclusters.[1–8] The structural response may be reflected in the complexation of the metal ion(s) with the surface ligands,[9–11] the doping/exchange/addition of the metal ion(s) into the metallic framework of the cluster,[12–15] the slightly changed structure with a different charge state[16] or the re-arrangement of the entire cluster structure.[17–20] Moreover, enhanced physicochemical properties (such as thermostability) and novel applications[21–23] could be achieved due to the synergistic effect.

Associated with the experimental outcomes, the atomic precision, spectroscopic characterization, and theoretical simulations have greatly improved our mechanistic understanding on these reactions. For example, the $[M^+]-Cl$ (M = Ag/Cu) interactions of the M^+ with the vertex AuCl moiety of the rod-shaped $Au_{24}(SR)_5(PR_3)_{10}Cl_2$ were found to be a dominating effect to initiate the single atom addition, and thus, the formation of the rod-shaped $Au_{24}M(SR)_5(PR_3)_{10}Cl_2$ clusters.[24] The Cs–S/O and cation–π interactions are pivotal to the Cs^+ induced one-dimensional linear assembly of $Ag_{29}(SSR)_{12}(PPh_3)_4$.[25] In addition, the anti-galvanic mechanism was proposed to account for the cation-stimulated alloying.[26–28] Nevertheless, the reported mechanistic study mainly focuses on the metal ion-induced alloying/assembly, while the mechanistic details on the ion "catalyzed" size conversion of nanoclusters (Ag^+ induced $[Au_6(dppp)_4]^{2+}$ to $[Au_7(dppp)_4]^{3+}$ and Cu^{2+} induced $Au_{25}(PET)_{18} \rightarrow Au_{44}(PET)_{18}$)[18,23] have been largely unknown.

Intrigued by the fantastic foreign metal effect,[29–31] we sought to perform a detailed mechanistic study on the Ag^+ induced reaction of $[Au_6(dppp)_4]^{2+} \rightarrow [Au_7(dppp)_4]^{3+}$ with density functional theory (DFT) calculations. According to Konishi's experiments,[18] $[Au_6(dppp)_4]^{2+}$ transformed into $[Au_7(dppp)_4]^{3+}$ within one minute after 5 molars equivalent $AgBF_4$ was added. According to single-crystal structure analysis, $[Au_6(dppp)_4]^{2+}$ comprises a bi-capped tetrahedral skeleton. The tetrahedral Au atoms (Au^{1-4}) are each protected by one P hand of the dppp ligand, while the two-terminal Au atoms ($Au^{5,6}$) are each protected by two P hands from two dppp ligands. The framework of $[Au_7(dppp)_4]^{3+}$ is similar to that of $[Au_6(dppp)_4]^{2+}$, except for the addition of one formal Au^+, and the re-arrangement of one dppp ligand (one P coordination on the Au^6 atom migrates to coordinate to Au^7).

According to the DFT calculation results, the addition of Ag^+ on clusters favorably generates the alloy structure with higher

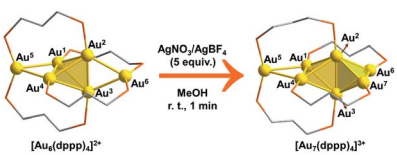

Scheme 1 The Ag^+ induced size-conversion of $[Au_6(dppp)_4]^{2+}$ to $[Au_7(dppp)_4]^{3+}$. The phenyl groups on the P atoms of dppp and the counter anion were omitted in both clusters. Color legends: Au, gold; P, orange; C, gray; H, omitted.

[a]*Department of Chemistry and Centre for Atomic Engineering of Advanced Materials, Anhui Province Key Laboratory of Chemistry for Inorganic/Organic Hybrid Functionalized Materials, Key Laboratory of Structure and Functional Regulation of Hybrid Materials of Ministry of Education, Anhui University, Hefei 230601, Anhui, P. R. China. E-mail: yuhaizhu@ahu.edu.cn*

[b]*Institute of Energy, Hefei Comprehensive National Science Center, Hefei, 230031, Anhui, P. R. China*

† Electronic supplementary information (ESI) available. See https://doi.org/10.1039/d2na00301e

nucleation (*i.e.* with more tetrahedral and triangular blocks in the core structure). The incorporated Ag^+ induced activation of the exterior Au atoms in the metal framework, resulting in an easy structural tautomerization therein. This proposal correlates with the heavily doping-induced size-rearrangement of metal nanoclusters in recent studies[27,32] and will be hopefully applicable to other alloying systems (Scheme 1).[18]

Results and discussion

Throughout this study, the experimentally used dppp ligands (*i.e.* bis(diphenylphosphino)propane) were simplified with dmpp (*i.e.* bis(dimethylphosphino)propane ligands) to reduce computational costs. Similar structural simplification has also been used in recent studies.[33,34]

The doping of Ag^+ in Au_6P_8 clusters

The formula of **Au_6P_8** is differentiated from **Au_7P_8** by only one Au^+, which is unlikely to be released directly from the Au_6P_8 precursor. To this end, the dissociation of Au^+ is anticipated to be induced by the Ag^+ doping of Au_6P_8. Given the high activity of the mono-nuclear, cationic Au^+ species, the generation of Au^+ from the gold cluster precursors is designated as the activation of the Au atom. Of note, the Ag^+ alloying-induced activation of the "Au" site(s) correlates with the general concept of anti-galvanic reduction.[26] Using Ag^+ as a dopant, we considered the possible configurations and energy demands for successive doping procedures.

Considering the structural symmetry and the Fukui function analysis (f^-, Fig. 1)[35] of the **Au_6P_8** precursor, the terminal $Au^{5/6}$ atom, $Au^{1/4}$-Au^5 bond, and $Au^{2/3}$-Au^6 bond are the most labile sites for the electrophilic attack of the first Ag^+. In this study, the isodesmic reaction of $\mathbf{NC}^{n+} + AgBF_4 \rightarrow [\mathbf{NCAg}]^{(n+1)+} + BF_4^-$ (**NC** denotes the reaction precursor for the Ag^+ addition steps) was used to determine the reaction energy of the Ag^+ addition steps. As shown in Fig. 1, the addition of the first Ag^+ could possibly generate **Au_6AgP_8-1** and **Au_6AgP_8-2**, and the suffix of **−1**/**−2** denotes the isomeric products *via* adding Ag^+ on different sites. Both two doping processes are thermodynamically highly feasible. Nevertheless, adding an exterior Ag^+ makes little perturbation on the Au^6 skeleton in the former case, but results in a stretched core structure in the latter case (Fig. 1 and S1†). From Fig. 1, the Au^4–Au^5 bond insertion is significantly more feasible than the Au^5-binding mode (−48.8 *vs.* −37.3 kcal mol^{-1}). Alternatively, Ag^+ is more likely to be reduced by Au_6; that is, Ag^+ is incorporated into the core sites to form a highly coordinated structure (the coordination number[36] of Ag^1 in **Au_6AgP_8-1** and **Au_6AgP_8-2** is 1 and 3; please see ESI† for more details), and thus **Au_6AgP_8-2** is preferentially formed.

According to the Hirshfeld charge analysis, the charge state of the terminal $Au^{5/6}$ in **Au_6P_8** (0.002/−0.009, Table S1†) is slightly higher than that of the tetrahedral Au (avg. −0.030). By contrast, the charge of Au^5 in **Au_6AgP_8-1** and **Au_6AgP_8-2** (0.055 and 0.057) is significantly more positive than that of tetrahedral Au atoms (avg. −0.012) and becomes closer to the charge of Au in the $Au_2(dppp)_2Cl_2$[37] complex (0.082). The results unambiguously demonstrate the improved positive charge of the Au^5 atom after Ag^+ incorporation, and thus the higher reactivity for bond dissociation (due to the increased electrostatic repulsion between the cationic metal centers). In other words, the incorporation of Ag^+ activates the core Au atoms, particularly in the corner sites.[38] Of note, compared to the aforementioned Ag^+-addition processes, the metal exchange of Ag with Au in **Au_6P_8** is thermodynamically much more disfavored (Scheme S1†). Therefore, the metal exchange pathways were not examined in the following section.

According to the Fukui function analysis, the most nucleophilic sites of **Au_6AgP_8-2** are located in the region nearby Au^5 and Au^6 atoms (Fig. 2). Accordingly, we examined four possible binding modes of the second Ag^+.

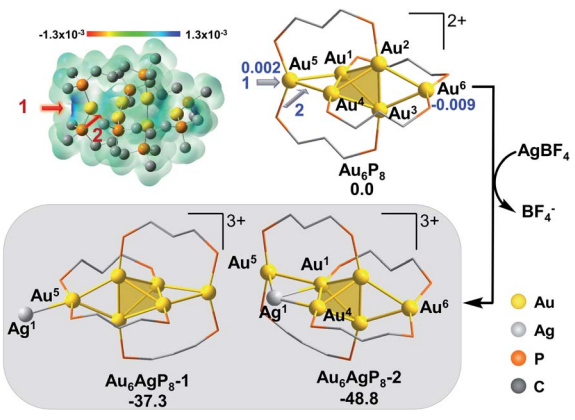

Fig. 1 The isosurface of the f^- for Au_6P_8, using the width of Gaussian function of 0.01 au, and the energy (in kcal mol^{-1}) and structural change for the doping of first Ag^+ into Au_6P_8. The Hirshfeld charge of $Au^{5/6}$ in the starting structure is given in blue and bold.

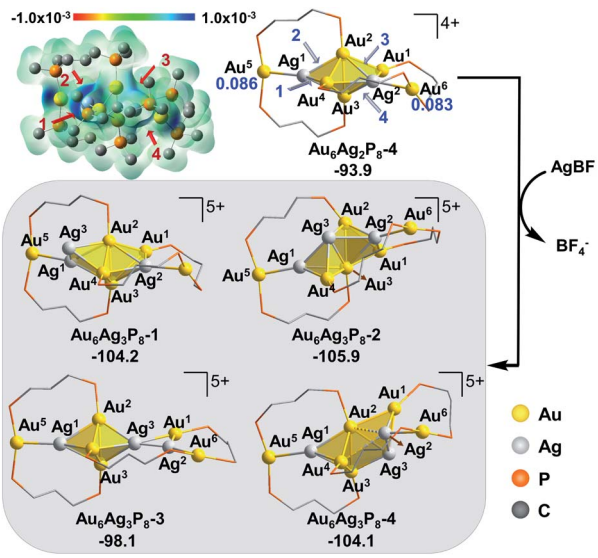

Fig. 2 The isosurface of the f^- for Au_6AgP_8-2, using the width of Gaussian function of 0.01 au and the energy (in kcal mol^{-1}) and structural changes for the doping of second Ag^+ into **Au_6AgP_8-2**. The Hirshfeld charge of $Au^{5/6}$ in the starting structure is given in blue and bold.

As shown in Fig. 2, the activation of the terminal Au^5 could occur *via* the addition of Ag^+ on the site 1 of Au^5 or site 2 of attacking the Au^2–Ag^1 bond to form the isomeric **$Au_6Ag_2P_8$-1** and **$Au_6Ag_2P_8$-2**, respectively. Similarly, the corner Au^6 could be possibly activated *via* Ag^+ insertion into the space behind (site 3) or in front (site 4) of the butterfly-like $Au^{1/4}$-Au^2-Au^3-Au^6 structure to form **$Au_6Ag_2P_8$-3** or **$Au_6Ag_2P_8$-4**.

The results indicate that the binding of second Ag^+ (*i.e.* Ag^2) directly on Au^5 makes little perturbation on the framework, correlating with the results of **Au_6P_8** + $AgBF_4$ → **Au_6AgP_8-1** + BF_4^- (Fig. 1). Nevertheless, the reaction energy is remarkably higher (−5.4 kcal mol^{-1} in **Au_6AgP_8-2** + $AgBF_4$ → **$Au_6Ag_2P_8$-1** *vs.* −37.3 kcal mol^{-1} in **Au_6P_8** + $AgBF_4$ → **Au_6AgP_8-1** + BF_4^-), implying that the structure of the precursor is pivotal to the facilitation of alloying. Moreover, the attack of Ag^2 to Ag^1 resembles a synergistic bi-molecular electrophilic reaction mechanism as the Au^1 atom migrates from *cis*-to *trans*-configuration (refer to Au^4) around the Au^2–Au^3 bond spontaneously during the geometry optimization (see Fig. S2† for the details). The formation of **$Au_6Ag_2P_8$-2** from **Au_6AgP_8-2** is exothermic by 30.7 kcal mol^{-1}. Besides, the approaching of Ag^2 to either Au^1–Au^2–Au^3–Au^6 or Au^4–Au^2–Au^3–Au^6 results in a core-structure re-organization, predominantly *via* incorporating Ag^1 into the tetrahedral blocks and forming the face-sharing tri-tetrahedral structure. Due to the meta-orientation of the two Ag^+ and the symmetry of the tri-tetrahedral core structure, the relative energy and the M-P framework of the formed **$Au_6Ag_2P_8$-3** are almost the same as those of **$Au_6Ag_2P_8$-4**. Both steps are highly exothermic (−44.8 and −45.1 kcal mol^{-1}). Through the structural re-organization, the reduced coordination number of Au^5 and Au^6 (compared to the related one in the precursor) is overwhelmed by the extra stability associated with the formation of a larger metallic core structure. Therefore, the formation of **$Au_6Ag_2P_8$-3/4** is favored over that of **$Au_6Ag_2P_8$-1/2**.

Comparing the optimized geometries of **Au_6AgP_8-2** and **$Au_6Ag_2P_8$-3/4**, we found that the bond distance between the Au^5/Au^6 and the core metal atoms is significantly lengthened after incorporating the second Ag^+. Moreover, the charge on Au^5/Au^6 atoms becomes more positive (**Au_6AgP_8-2**: 0.057/0.035 → **$Au_6Ag_2P_8$-2**: 0.086/0.083, Table S1†), and is comparable to that of the aforementioned Au(I) complex (0.082). The results indicate the formation of a formal Au(I) center on the cluster, and thus, the enhanced activity for the nucleophilic coordination and Au–Au dissociation (the charge of the other Au atoms also becomes more positive, Table S1†). Nevertheless, the alloying with Ag^+ remains thermodynamically feasible, and therefore, we examined the energetics for further doping of Ag^+ in the target system.

In view of the preferential core expansion *via* Ag^+ doping (over the Ag addition steps), we mainly examined the core-expansion pathways from **$Au_6Ag_2P_8$-4**. As shown in Fig. 3, the third Ag-doping process leads to four possible $Au_6Ag_3P_8$ isomers. The third Ag^+ (*i.e.* Ag^3) could possibly attack site 1 of the Ag^1–Au^4 bond, site 2 of the Au^2–Ag^1 bond, site 3 of the Au^2–Ag^2 bond, and site 4 of the Ag^2–Au^3 bond, forming **$Au_6Ag_3P_8$-1**, **$Au_6Ag_3P_8$-2**, **$Au_6Ag_3P_8$-3**, and **$Au_6Ag_3P_8$-4**, respectively. The approaching of Ag^3 into the Ag^1–Au^4 bond internalizes Ag^3 into

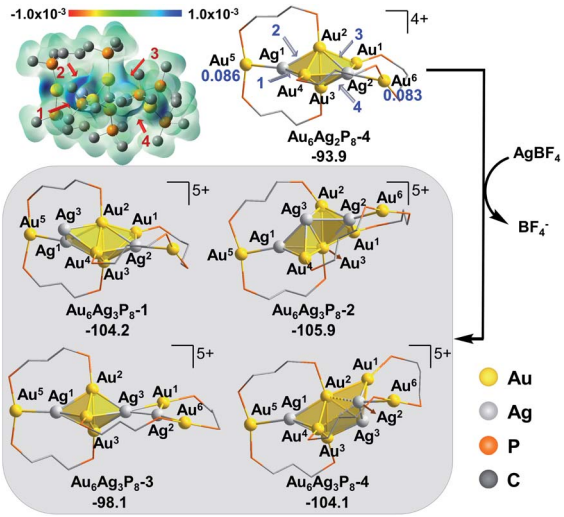

Fig. 3 The f^- isosurface of $Au_6Ag_2P_8$-4, using the width of Gaussian function of 0.01 au, and the energy (in kcal mol^{-1}) and structure change after doping of the third Ag^+ into $Au_6Ag_2P_8$-4. The Hirshfeld charge of $Au^{5/6}$ in the starting structure is given in blue and bold.

the left tetrahedral $Ag^1Au^{2,3,4}$ block, forming a square pyramid ($Ag^{1,3}Au^{2,3,4}$) therein. Moreover, the approaching of Ag^3 to the Au^2–Ag^1 bond results in the enlargement of the Au^2–Au^3–Ag^1/Au^4 bond angle, and the incorporation of Ag^3 to form two vertex-sharing tetrahedral blocks (see Fig. S3† for the partial optimization energy profile). The approaching of Ag^3 to the Au^2–Ag^2 bond leads to the extrusion of the Au^1–Au^2 bond from the metallic core structure, resulting in the formation of a face-sharing bi-tetrahedral block with a vertex-sharing triangular $Au^1Ag^{2,3}$ unit (**$Au_6Ag_3P_8$-3**). The attack of Ag^3 on the Ag^2-Au^3 bond results in the formation of a distorted square-pyramid $Au^{2,3}Ag^{2,3,4}$ block, and the cleavage of the Au^1/Ag^2–Au^3 bonds. In the formed **$Au_6Ag_3P_8$-4**, the new-formed square-pyramid shares one facet with the original left tetrahedron. According to the calculation results, the four types of Ag^+ insertion steps are exothermic by 10.3, 12.0, 4.2, and 10.2 kcal mol^{-1}, respectively.

The slightly higher energy of **$Au_6Ag_3P_8$-3** than the other isomers is predominantly caused by the lower cohesive degree of the whole metal skeleton[39] (the average coordination number of the metal atoms is 3.4/3.4/3.1/3.3 for **$Au_6Ag_3P_8$-1/2/3/4**, see details in Table S2†).[36] In addition, the comparable energies of **$Au_6Ag_3P_8$-1**, **$Au_6Ag_3P_8$-2**, and **$Au_6Ag_3P_8$-4** indicate the competitive Ag^+ doping sites. For clarity reasons, the following analysis and discussions mainly refer to the most stable intermediate **$Au_6Ag_3P_8$-2**.

According to Hirshfeld charge analysis, the doping with the third Ag^+ further enhances the electron deficiency of the Au^5/Au^6 atoms (with the charge of 0.114/0.109, compared to the charge of 0.086/0.083 in **$Au_6Ag_2P_8$-4**, Table S1†). Moreover, the average charge of the Au_4Ag_n (Au_4 denotes the tetrahedral Au_4 block in the Au_6 reactant, and n = 1–4) blocks also significantly increases with the doping with the third Ag^+ (**Au_6P_8**: −0.030 → **Au_6AgP_8-2**: −0.012 → **$Au_6Ag_2P_8$-4**: 0.019 → **$Au_6Ag_3P_8$-4**: 0.070),

resulting in critically increased electrostatic repulsion within the metal skeleton and the reduced stability. This is also the reason why the Ag^+ doping becomes less feasible after each doping process (the first, second, and third Ag^+ doping steps are exothermic by −48.8, −45.1, and −12.0 kcal mol^{-1}).

Starting from **$Au_6Ag_3P_8$-2**, the fourth Ag^+ (*i.e.* Ag^4) could be capped on the $Ag^{1,3}Au^4$ facet as the maximum of f^- appears above the $Ag^{1,3}Au^4$ facet, and then the four-Ag^+-doped product **$Au_6Ag_4P_8$-1** was formed.

The incorporation of Ag^4 also resembles a synergistic bi-molecular electrophilic reaction mechanism, similar to the reaction of **Au_6AgP_8-2** + $AgBF_4$ → **$Au_6Ag_2P_8$-2**. When the Ag^4 atom is capped on the bare $Ag^{1,3}Au^4$ facet, the Au^3 atom leaves the back capping site (on the $Ag^{1,3}Au^4$ facet) with the right part of the face-sharing bi-tetrahedron remaining. Distinct from the aforementioned exothermic doping processes in the 1–3 Ag^+ incorporation steps, adding the fourth Ag^+ *via* this pathway was endothermic by 3.8 kcal mol^{-1} (Fig. 4). In other words, the incorporation of the fourth Ag^+ is thermodynamically disfavored. The reason is mainly ascribed to the significantly enhanced electrostatic repulsion among the metal atoms (the average Hirshfeld charge of the metal atoms in the Au_4Ag_n core is 0.112 for **$Au_6Ag_4P_8$-1**). Throughout the Ag-doping pathway, Ag^+ favors the core site of Au_6Ag_n and leads to the oxidation of Au atoms (*i.e.* $Au^{5,6}$). As shown in Scheme S2,† the contribution of Ag^+ to the HOMO of Au_6Ag_n (n = 0, 1, 2, and 3) increased remarkably with the increased doping number of Ag^+ (Au_6: 0.00%, Au_6Ag: 21.74%, Au_6Ag_2: 41.27%, and Au_6Ag_3: 43.05%). In combination with the Fukui function analysis (Fig. 1–4), the Au sites adjacent to Ag atoms are the active sites for the electrophilic attack of the incoming-Ag^+.

Size-growth by the dimerization of $Au_6Ag_3P_8$-2

According to the aforementioned results and discussion, the successive addition of Ag^+ on **Au_6P_8** favorably generates the alloy structure with a higher degree of nucleation (*i.e.* with more tetrahedral and triangular blocks in the core structure).[40] Meanwhile, the most plausible doping number of Ag^+ is 3 (**Au_6P_8** + 3 $AgBF_4$ → **$Au_6Ag_3P_8$-2** + 3 BF_4^-), wherein the metallic core has been largely activated due to the strong electrostatic repulsion therein (most Au atoms show Au(I) character, Table S1†). In this context, the terminal Au^5 and Au^6 atoms are the most labile sites for the subsequent reactions because of the relatively lower steric hindrance and the higher electron deficiency (compared to all other metal sites). For this reason, the Au^5 (or Au^6) in **$Au_6Ag_3P_8$-2** is used as the $[Au]^+$ source to react with the **Au_6P_8** cluster precursor to form **Au_7P_8**.

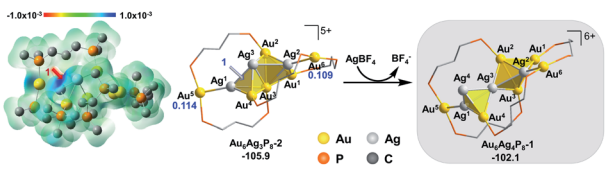

Fig. 4 The isosurface of the f^- for $Au_6Ag_3P_8$-2, using the width of Gaussian function of 0.01 au, and the energy (in kcal mol^{-1}) and structure changes after doping of the fourth Ag^+ into $Au_6Ag_3P_8$-2. The Hirshfeld charge of $Au^{5/6}$ in the starting structure is given in blue and bold.

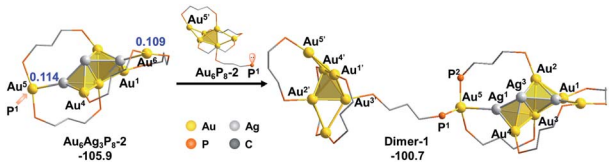

Fig. 5 The energy (in kcal mol^{-1}) and structural changes after the reaction of Au_6P_8-2 with $Au_6Ag_3P_8$-2. The labels Au^n and $Au^{n'}$ denote the same Au sites from the two Au_6P_8 reactants. The Hirshfeld charge of terminal Au is given in blue and bold.

Of note, the direct approaching of **$Au_6Ag_3P_8$-2** to **Au_6P_8** is precluded due to the high inter-cluster steric hindrance (see Fig. S4;† note: the steric hindrance would be much higher for the experimental dppp protected system). In this context, a prior Au^5–P dissociation on **Au_6P_8** (**Au_6P_8** → **Au_6P_8-2**, see Fig. S5†) might occur first to release the steric hindrance.[34] After that, the nucleophilic attack of P^1 to Au^5 occurs with the formation of **Dimer-1** (Fig. 5), and this step is slightly endothermic by 5.2 kcal mol^{-1}. By contrast, the coordination of P^1 to the Au^6 atom is thermodynamically slightly less disfavored (6.7 kcal mol^{-1}, Scheme S3†); thus, its subsequent transformations were omitted for clarity reasons. The P–Au bonding makes no obvious influence on the framework of both cluster precursors. To this end, the endothermicity might be caused by the high steric hindrance around the over-protected Au^5 (coordination number: 4, with three P-coordination).

Given the high steric hindrance around Au^5, the adjacent bare Ag^1 in **Dimer-1**, and the easiness for 1,2 P migration in cluster systems,[41–43] we examined the possibility of a 1,2-P^2 migration from Au^5 to Ag^1. The kinetic analysis by partial optimization (*via* gradually shortening the P^2–Ag^1 bond distance; see Fig. S6† for details) demonstrates the gradual bond cleavage of Au^5–Ag^1 and Au^3–Ag^2 bonds. As a result, the triangular bi-pyramidal block of $Au^{1,2,3}Ag^{2,3}$ (Fig. 6, inset) tautomerizes into a twisted square pyramid. The energy curve indicates a low energy barrier (12.4 kcal mol^{-1}, Fig. S6†), which could be easily overcome under the experimental condition (*i.e.* room temperature).[18] Meanwhile, due to the released steric

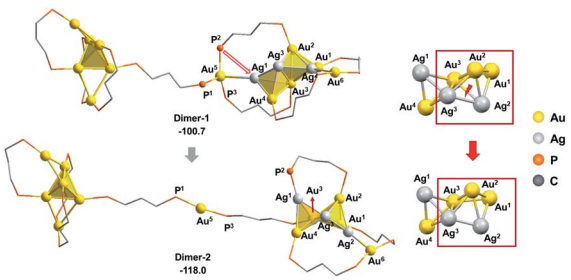

Fig. 6 The energy (in kcal mol^{-1}) and structural changes after the P^2-migration of **Dimer-1**, and the details of the tautomerized core structure.

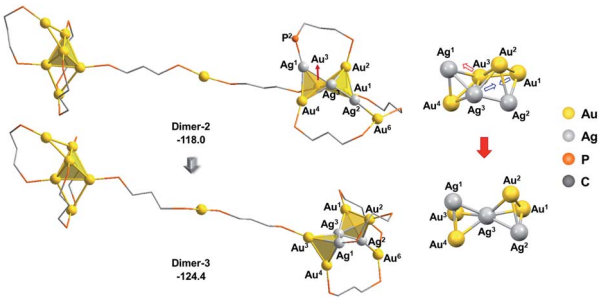

Fig. 7 The isomerization of the alloy core in **Dimer-2**. The relative energies are given in kcal mol^{-1}. The methyl groups on the dmpp ligands and all H atoms are omitted for clarity reasons.

hindrance around the Au^5 atom, the concerned P^2-migration from **Dimer-1** to **Dimer-2** is exothermic by 17.3 kcal mol^{-1}.

As the square pyramid block has been found to be less stable than the triangular bipyramid block (**$Au_6Ag_3P_8$-1** *vs.* **$Au_6Ag_3P_8$-2**, Fig. 3), we further examined an isomerization of **Dimer-2** *via* changing the square pyramidal block into a triangular bipyramidal one (**Dimer-3** in Fig. 7).[40] This isomerization was found to occur easily *via* lengthening the Au^1–Au^3 bond distance, with a barrier of 8.0 kcal mol^{-1} (Fig. S7†). The relative energy of **Dimer-3** is lower than that of **Dimer-2** by 6.4 kcal mol^{-1}, demonstrating the thermodynamic facility of this step.

From **Dimer-3**, the approaching of the Au^5 atom to the Au_6 block is requisite to forming the target Au_7 structure, which could be regulated by a series of single bond rotation processes of the related dmpp ligand (**Dimer-3** → **Dimer-6** in Scheme 2; see Fig. S8† for the details). Throughout the transformations, the structure of the alloy moiety is preserved, and the system energy is decreased by 7.5 kcal mol^{-1}.

From **Dimer-6**, the target Au_7 block of **Au_7P_8** could be formed *via* the binding of Au^5 to the Au$^{1',4',5'}$ facet of the Au_6 block, and the dissociation of the Au^5–P^3 bond (Fig. 8). According to the calculation results, the binding of Au^5 is exothermic by 3.2 kcal mol^{-1} and occurs with a very low barrier of <5 kcal mol^{-1} (Fig. S9†). From **Dimer-7**, the Au^5–P^3 cleavage

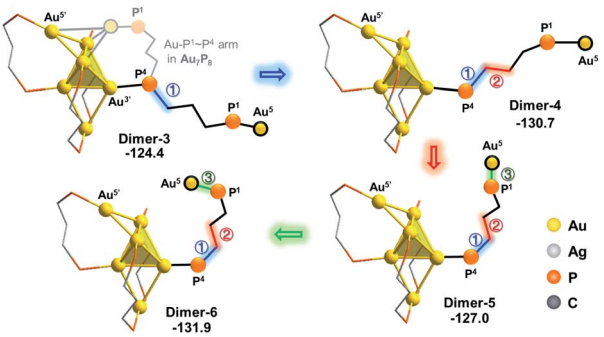

Scheme 2 Illustrative diagram for the structural tautomerization of the transformation of **Dimer-3** to **Dimer-6** (the relative energies are given in kcal mol^{-1}). The alloy block away from Au^5 was omitted for clarity reasons.

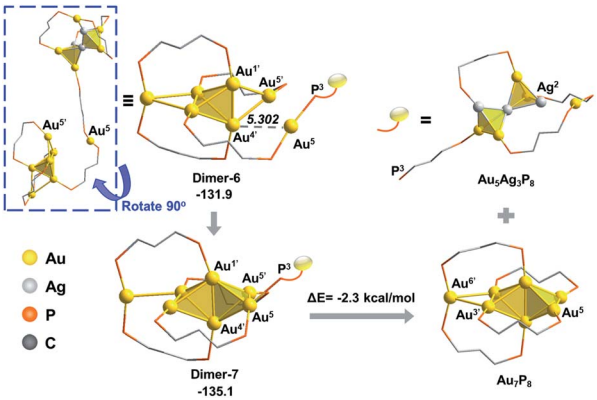

Fig. 8 The formation of the Au_7 skeleton from **Dimer-6** to **Dimer-7** and the subsequent Au^5–P^3 cleavage step. The relative energies are given in kcal mol^{-1}.

occurs to generate **Au_7P_8** and a by-product **$Au_5Ag_3P_8$**. In contrast, the progress of moving an Ag$^+$ from **$Au_6Ag_3P_8$-3** to **Au_6P_8** to generate **Au_6AgP_8** is thermodynamically less feasible (−18.7 kcal mol^{-1}, see exothermic by only 2.3 kcal mol^{-1}. The total reaction energy of **Au_6P_8** + **$Au_6Ag_3P_8$-3** → **Au_7P_8** + **$Au_5Ag_3P_8$** is −31.4 kcal mol^{-1}. See Scheme S3† for more details), demonstrating that the alloy cluster after Ag$^+$ doping is a good [Au]$^+$ donor, but not a good [Ag]$^+$ donor.

Due to the lack of experimental evidence and the complexity of the reaction system, we are not able to confirm the final state of Ag at this stage. However, in view of the bare Ag^2 atom and the dangling P^3 atom, we assumed that **$Au_5Ag_3P_8$** could possibly undergo the P^3–Ag^2 coordination to generate a more stable intermediate. The calculation results (**$Au_5Ag_3P_8$** → **$Au_5Ag_3P_8$-2**, Scheme S4†) indicate this step to be highly feasible (exothermic by 26.8 kcal mol^{-1}). In particular, after the Au–P coordination, the Au_6 atom was further extruded from the metallic core and could possibly act as the second "[Au]$^+$" source to regulate the second **Au_6P_8** → **Au_7P_8** conversion. The formed **$Au_4Ag_3P_8$** could undergo further Ag–P coordination (Scheme S4†) or comprehensive nucleation/decomposition processes. Due to the complexity of the target reaction system, the details for the conversion of **$Au_5Ag_3P_8$** are still ambiguous and deserve more studies.

Experimentally, $AgBF_4$ was not largely excessive, and thus, the transformation from **Au_6P_8** to **Au_7P_8** might deviate from a pseudo-first-order reaction. Hence, the reaction pathways using **Au_6AgP_8-2** and **$Au_6Ag_2P_8$-4** as [Au$^+$] sources were also examined. As shown in Scheme S5,† the Au$^+$ migration from **Au_6AgP_8-2** or **$Au_6Ag_2P_8$-3** to the Au_6 skeleton was as feasible as that from **$Au_6Ag_3P_8$-3** (energy demands are all lower than 15 kcal mol^{-1}). According to the aforementioned results and discussion, the Ag$^+$ induced size conversion from **Au_6P_8** to **Au_7P_8** could occur *via* a series of competitive pathways. For clarity, the most feasible pathway deduced in this study is shown in Scheme 3 (the relative energies are given with the reference states of **Au_6P_8** and $AgBF_4$).

In this mechanism, the continuous doping of **Au_6P_8** clusters with Ag$^+$ (dominant doping product: **$Au_6Ag_3P_8$-2**) activates the terminal Au atoms and generates the [Au]$^+$ source for

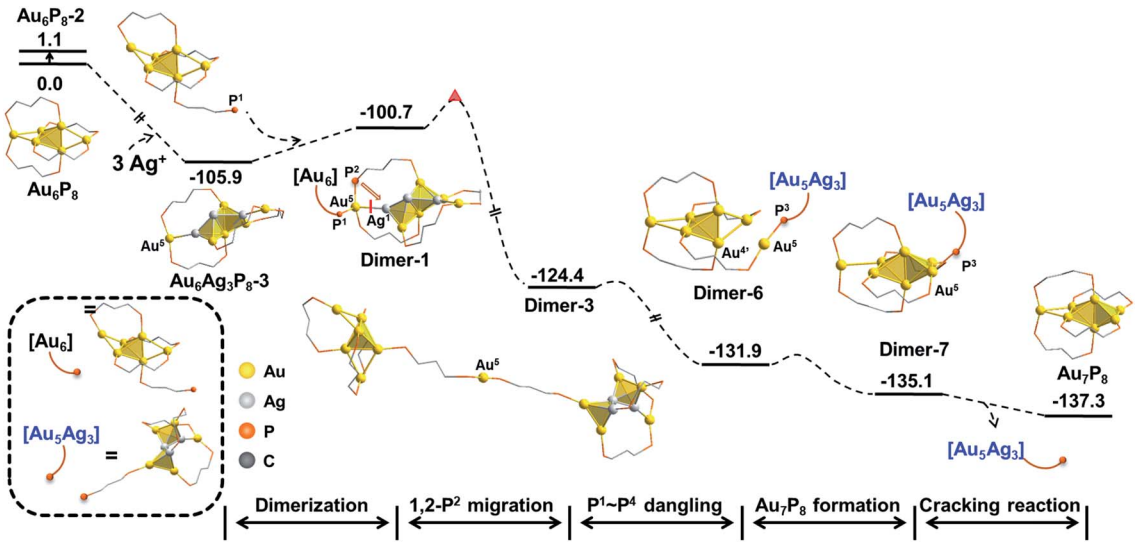

Scheme 3 The total energy profile of Ag^+ catalyzed size-growth of Au_6P_8 to Au_7P_8. The relative energies are given in kcal mol^{-1}.

subsequent size conversion. After that, Au–P coordination between the dangling phosphine ligand of the Au_6 precursor and the formal [Au^+] occurs, followed by the intramolecular migration of [Au^+] through a series of isomerization steps (on the diphosphine ligand). Finally, the **Au_7P_8** product is formed *via* the Au–P dissociation and the release of the alloy cluster block. Albeit the comprehensive calculations, the experimental evidence for the proposed mechanism is still lacking, predominantly due to the rapid reaction rate and the lability of the formed $[Au_7(dppp)_4](BF_4)_3$ to convert to $[Au_8(dppp)_4Cl_2]$.[33,34] Moreover, some other mechanistic possibilities, such as the formation of the target Au_7 products *via* the reaction of one alloy intermediate with another one, could not be excluded.

Computational details

The modeling clusters were constructed by simplifying the dppp ligands with dmpp ligands. Geometry optimization of all species was performed with Dmol^3 software[44] with the generalized gradient approximation[45–47] Perdew–Burke–Ernzerhof functional.[48–50] Effective core potentials and double numerical orbital basis group + orbital polarization function (DNP) base groups (Basic 4.4) were chosen with the values of 2×10^{-5} Ha for total energy, 0.004 Ha $Å^{-1}$ for force, 0.05 Å for displacement, and 1×10^{-5} Ha for the self-consistent field (SCF) computation criterion. Following the recent studies,[51–54] the constrained structural optimization strategy is used in evaluating the barrier of the elementary steps. Based on the optimized structures, the solution-phase single point energy calculations were conducted with the COSMO[55,56] model, using methanol as the solvent (corresponding to Konishi's experimental conditions[18]). Unless otherwise specified, the solution-phase binding energy (in kcal mol^{-1}) was used to determine the energy changes of all steps. The Fukui function of the f^- evaluated using finite difference approximations and the orbital composition analysis of the metal skeleton was calculated with Multiwfn version 3.8.[35,57,58]

Conclusions

Herein, a plausible mechanism for the Ag^+ induced conversion from $[Au_6(dppp)_4]^{2+}$ to $[Au_7(dppp)_4]^{3+}$ was proposed with DFT calculations. The size growth starts with the successive doping of Ag^+ (preferentially adopts high nucleation), associated with the gradual formation of formal Au(I) on terminal sites and the weakened metal–metal bonding interactions. In this context, the release of the terminal Au atom (*i.e.* the activated Au(I) atom) to the Au_6 precursor occurs easily to generate the Au_7 cluster product, while the alloy cluster could further function as a "Au(I)" donor to regulate another group of the **$Au_6P_8 \rightarrow Au_7P_8$** conversion. Due to the complexity of the target reaction system, the full details on the overall size growth remain to be established. Nevertheless, the mechanism insights, such as the preferential doping site of Ag^+ on the cluster precursor (on the most nucleophilic site, and favorably forms structures with a higher degree of nucleation), the activation of exterior Au atom(s) *via* the gradual incorporation of Ag^+ (*i.e.* formation of formal Au(I) and its subsequent dissociation, re-assembly, *etc.*), and the easy structure tautomerization in the metallic core and the diphosphine ligands, will be helpful for understanding the inherent correlation between different nanoclusters and their alloying reactivity in future studies.

Author contributions

H. Y. conceived and supervised the project. Y. L. carried out the experimental planning, simulations, and data analysis. X. W. and S. H. provided constructive suggestions.

Conflicts of interest

There are no conflicts to declare.

Acknowledgements

We acknowledge financial support from National Science Foundation of Anhui Province (2108085J08), The University Synergy Innovation Program of Anhui Province (GXXT-2021-023), 2021 university scientific research projects of Anhui Province (YJS20210031), and the technical support of high-performance computing platform of Anhui University. Super-computing facilities were provided by the Hefei Advanced Computing Center.

Notes and references

1 A. George, A. Sundar, A. S. Nair, M. P. Maman, B. Pathak, N. Ramanan and S. Mandal, *J. Phys. Chem. Lett.*, 2019, **10**, 4571–4576.
2 S. Li, Z. Y. Wang, G. G. Gao, B. Li, P. Luo, Y. J. Kong, H. Liu and S. Q. Zang, *Angew. Chem., Int. Ed.*, 2018, **57**, 12775–12779.
3 Z. J. Guan, F. Hu, J. J. Li, Z. R. Wen, Y. M. Lin and Q. M. Wang, Isomerization in Alkynyl-Protected Gold Nanoclusters, *J. Am. Chem. Soc.*, 2020, **142**, 2995–3001.
4 L. L. Yan, L. Y. Yao, M. Ng and V. W. Yam, *J. Am. Chem. Soc.*, 2021, **143**, 19008–19017.
5 J. M. Lopez-de-Luzuriaga, M. Monge, M. E. Olmos, J. Quintana and M. Rodriguez-Castillo, *Inorg. Chem.*, 2019, **58**, 1501–1512.
6 Y. Zhao, M. Yu, C. Liu, S. Li, Z. Li, F. Jiang, L. Chen and M. Hong, *J. Mater. Chem. C*, 2021, **9**, 2890–2897.
7 Y. Yuan, K. Sheng, S. Zeng, X. Han, L. Sun, I. Loncaric, W. Zhan and D. Sun, *Inorg. Chem.*, 2020, **59**, 5456–5462.
8 N. Yan, L. Liao, J. Yuan, Y.-j. Lin, L.-h. Weng, J. Yang and Z. Wu, *Chem. Mater.*, 2016, **28**, 8240–8247.
9 N. Yan, N. Xia and Z. Wu, *Small*, 2021, **17**, 2000609.
10 Z. Liu, X. Jing, S. Zhang and Y. Tian, *Anal. Chem.*, 2019, **91**, 2488–2497.
11 Q. Zhou, Y. Lin, M. Xu, Z. Gao, H. Yang and D. Tang, *Anal. Chem.*, 2016, **88**, 8886–8892.
12 J. Lin, Q. Zhang, L. Wang, X. Liu, W. Yan, T. Wu, X. Bu and P. Feng, *J. Am. Chem. Soc.*, 2014, **136**, 4769–4779.
13 C. Yao, J. Chen, M. B. Li, L. Liu, J. Yang and Z. Wu, *Nano Lett.*, 2015, **15**, 1281–1287.
14 M. Kim, K. L. D. M. Weerawardene, W. Choi, S. M. Han, J. Paik, Y. Kim, M.-G. Choi, C. M. Aikens and D. Lee, *Chem. Mater.*, 2020, **32**, 10216–10226.
15 R. P. B. Silalahi, Q. Wang, J. H. Liao, T. H. Chiu, Y. Y. Wu, X. Wang, S. Kahlal, J. Y. Saillard and C. W. Liu, *Angew. Chem., Int. Ed.*, 2022, **61**, e202113266.
16 M. Zhu, G. Chan, H. Qian and R. Jin, *Nanoscale*, 2011, **3**, 1703–1707.
17 P. K. Liao, C. S. Fang, A. J. Edwards, S. Kahlal, J. Y. Saillard and C. W. Liu, *Inorg. Chem.*, 2012, **51**, 6577–6591.
18 Y. Shichibu, M. Zhang, Y. Kamei and K. Konishi, *J. Am. Chem. Soc.*, 2014, **136**, 12892–12895.
19 C. Yao, Y. J. Lin, J. Yuan, L. Liao, M. Zhu, L. H. Weng, J. Yang and Z. Wu, *J. Am. Chem. Soc.*, 2015, **137**, 15350–15353.
20 S. Lee, M. S. Bootharaju, G. Deng, S. Malola, H. Hakkinen, N. Zheng and T. Hyeon, *J. Am. Chem. Soc.*, 2021, **143**, 12100–12107.
21 R. Jiang, Y. Zhang, Q. Zhang, L. Li and L. Yang, *ACS Appl. Nano Mater.*, 2021, **4**, 9760–9767.
22 L. Liao, S. Zhou, Y. Dai, L. Liu, C. Yao, C. Fu, J. Yang and Z. Wu, *J. Am. Chem. Soc.*, 2015, **137**, 9511–9514.
23 M. B. Li, S. K. Tian, Z. Wu and R. Jin, *Chem. Commun.*, 2015, **51**, 4433–4436.
24 S. Wang, H. Abroshan, C. Liu, T.-Y. Luo, M. Zhou, H. J. Kim, N. L. Rosi and R. Jin, Shuttling single metal atom into and out of a metal nanoparticle, *Nat. Commun.*, 2017, **8**, 848.
25 X. Wei, X. Kang, Q. Yuan, C. Qin, S. Jin, S. Wang and M. Zhu, *Chem. Mater.*, 2019, **31**, 4945–4952.
26 Z. Wu, Anti-Galvanic Reduction of Thiolate-protected Gold and Silver Nanoparticles, *Angew. Chem., Int. Ed.*, 2012, **51**, 2934–2938.
27 M. Zhu, P. Wang, N. Yan, X. Chai, L. He, Y. Zhao, N. Xia, C. Yao, J. Li, H. Deng, Y. Zhu, Y. Pei and Z. Wu, *Angew. Chem., Int. Ed.*, 2018, **57**, 4500–4504.
28 X. Liu, J. Yuan, J. Chen, J. Yang and Z. Wu, *Part. Part. Syst. Charact.*, 2019, **36**, 1900003.
29 X. Lin, W. Ma, K. Sun, B. Sun, X. Fu, X. Ren, C. Liu and J. Huang, *J. Phys. Chem. Lett.*, 2021, **12**, 552–557.
30 F. Tian and R. Chen, *J. Am. Chem. Soc.*, 2019, **141**, 7107–7114.
31 A. K. Das, S. Mukherjee, S. R. Sreehari, A. S. Nair, S. Bhandary, D. Chopra, D. Sanyal, B. Pathak and S. Mandal, *ACS Nano*, 2020, **14**, 16681–16688.
32 Y. Negishi, T. Iwai and M. Ide, *Chem. Commun.*, 2010, **46**, 4713–4715.
33 Y. Kamei, Y. Shichibu and K. Konishi, *Angew. Chem., Int. Ed.*, 2011, **50**, 7442–7445.
34 Y. Lv, R. Zhao, S. Weng and H. Yu, *Chem. – Eur. J.*, 2020, **26**, 12382–12387.
35 P. Geerlings, F. De Proft and W. Langenaeker, *Chem. Rev.*, 2003, **103**, 1793–1874.
36 C. Liu, Y. Pei, H. Sun and J. Ma, *J. Am. Chem. Soc.*, 2015, **137**, 15809–15816.
37 W. Kaim, A. Dogan, A. Klein and S. Záliš, *Z. Anorg. Allg. Chem.*, 2005, **631**, 1355–1358.
38 J. H. Stenlid and T. Brinck, *J. Am. Chem. Soc.*, 2017, **139**, 11012–11015.
39 M. G. Taylor and G. Mpourmpakis, *Nat. Commun.*, 2017, **8**, 15988–15995.
40 W. W. Xu, B. Zhu, X. C. Zeng and Y. Gao, *Nat. Commun.*, 2016, **7**, 13574–13581.
41 D. S. Matteson, *Chem. Rev.*, 1989, **89**, 1535–1551.
42 J. Q. Wang, Z. J. Guan, W. D. Liu, Y. Yang and Q. M. Wang, *J. Am. Chem. Soc.*, 2019, **141**, 2384–2390.
43 X. Wu, Y. Lv, Y. Bai, H. Yu and M. Zhu, *Dalton Trans.*, 2021, **50**, 10113–10118.
44 B. Delley, *J. Chem. Phys.*, 1990, **92**, 508–517.
45 J. P. Perdew, K. Burke and M. Ernzerhof, *Phys. Rev. Lett.*, 1996, **77**, 3865–3868.
46 J. P. Perdew, K. Burke and M. Ernzerhof, *Phys. Rev. Lett.*, 1997, **78**, 1396.

47 K. Weerawardene, P. Pandeya, M. Zhou, Y. Chen, R. Jin and C. M. Aikens, *J. Am. Chem. Soc.*, 2019, **141**, 18715–18726.
48 Q. Li, M. A. Mosquera, L. O. Jones, A. Parakh, J. Chai, R. Jin, G. C. Schatz and X. W. Gu, *ACS Nano*, 2020, **14**, 11888–11896.
49 J. V. Rival, P. Mymoona, R. Vinoth, A. M. V. Mohan and E. S. Shibu, *ACS Appl. Mater. Interfaces*, 2021, **13**, 10583–10593.
50 A. Klamt and G. Schuurmann, *J. Chem. Soc., Perkin Trans.*, 1993, **2**, 799–805.
51 M. F. Matus, S. Malola, E. Kinder Bonilla, B. M. Barngrover, C. M. Aikens and H. Hakkinen, *Chem. Commun.*, 2020, **56**, 8087–8090.
52 S. Malola and H. Hakkinen, *J. Am. Chem. Soc.*, 2019, **141**, 6006–6012.
53 A. Fernando and C. M. Aikens, *J. Phys. Chem. C*, 2015, **119**, 20179–20187.
54 C. L. Heinecke, T. W. Ni, S. Malola, V. Makinen, O. A. Wong, H. Hakkinen and C. J. Ackerson, *J. Am. Chem. Soc.*, 2012, **134**, 13316–13322.
55 A. Klamt, *J. Phys. Chem.*, 1995, **99**, 2224–2235.
56 A. Klamt and V. Jonas, *J. Chem. Phys.*, 1996, **105**, 9972–9981.
57 T. Lu and F. Chen, *J. Comput. Chem.*, 2012, **33**, 580–592.
58 T. Lu and F. Chen, *Acta Chim. Sin.*, 2011, **69**, 2393–2406.